



Cite this: *RSC Appl. Interfaces*, 2024,
1, 522

Submicron-thick single anion-conducting polymer electrolytes†

Hunter O. Ford, ^a Brian L. Chaloux, ^b Youngchan Kim,^c Jeffrey W. Long, ^b
Debra R. Rolison ^{*b} and Megan B. Sassin ^{*b}

Non-line-of-sight techniques are well suited for fabrication of thin and conformal solid-state electrolyte (SSE) coatings, especially within three-dimensionally porous electrode architectures. Adapting SSEs to safe and low supply-risk battery chemistries, such as alkaline zinc, requires solid-state anionic transport. We use initiated chemical vapor deposition (iCVD), a non-line-of-sight polymerization method, to generate conformal, pinhole-free poly(4-dimethylaminomethylstyrene), pDMAMS, films on planar substrates. We then vapor-phase react the ~350 nm thick polymer with 1-bromo-3-chloropropane, an alkylating and cross-linking reagent, to convert pendant tertiary amines in pDMAMS to quaternary ammoniums (pDMAMS⁺) counterbalanced by labile Cl[−]/Br[−]. Solution exchange of Cl[−]/Br[−] for OH[−] or HCO₃[−] yields an anion-conducting SSE compatible with alkaline battery chemistry. The ion conductivity of anion-compensated pDMAMS⁺ films ranges from 10^{−8} to 10^{−5} S cm^{−1} and depends on hydration level and anion identity. All three anionic forms of the pDMAMS⁺ SSEs are electrochemically stable and electronically insulating, which in conjunction with their nanoscale thickness and single-ion conductivity render them promising for use in beyond-Li-ion all solid-state energy-storage and conversion devices.

Received 18th December 2023,
Accepted 4th February 2024

DOI: 10.1039/d3lf00257h

rsc.li/RSCApplInter

Introduction

Meeting the high energy and power demands of future technologies requires transitioning from the 200+ years-old planar battery configuration to a 3D all-solid-state battery (3D SSB) configuration. Designing in 3D decouples the scaling of energy, power, and footprint, a feat that is physically impossible with the 2D planar battery design.¹ In the aperiodic 3D SSB design developed by Rolison and Long,^{1,2} the bulk of the 3D SSB volume is occupied by interpenetrating networks of cathode and anode that are physically separated by a submicron-thick solid-state electrolyte (SSE). Energy is increased within a given footprint by increasing the thickness of the battery without altering the characteristic dimensions of cathode, anode, and SSE, thereby maintaining short-range local ion transport that translates to high power.¹

Multiple 3D SSB examples in the literature validate the viability of scaling energy without sacrificing power in a small footprint,^{3–5} yet are restricted to microscale dimensions because they are based on conventional Li-ion materials that have limited thermal and electronic conductivity.^{4–6} These limitations inherent to reported 3D microbatteries can be circumvented by moving to battery chemistries with metallic electrodes, such as silver–zinc (Ag–Zn) in which both redox couples (Ag/AgO and ZnO/Zn) are orders of magnitude more thermally and electrically conductive than conventional Li-ion cathode active materials.^{7,8} Our development of a mechanically robust 3D Zn sponge^{9–12} that can serve as the scaffold of the 3D SSB enables macroscale 3D Ag–Zn SSBs. The crux to fabricating a Ag–Zn sponge 3D SSB is a thin, pinhole-free, anion-conducting SSE, which requires a robust method of non-line-of-sight deposition within the tortuous void network of the sponge.

An emerging technique for generating SSEs and other thin coatings for 3D SSBs is initiated chemical vapor deposition (iCVD), a non-line-of-sight method proven to conformally coat nanometric polymers on substrates with complex morphologies.^{13–20} For example, Chen and colleagues generate a 10–40 nm thick Li⁺-conducting SSE with ionic conductivity on the order of 10^{−8} S cm^{−1} by iCVD coating high aspect-ratio nanowires with poly(tetravinyltetramethylcyclotetrasiloxane, poly-V4D4) and doping with Li salts.¹⁵

^a NRL–NRC Postdoctoral Associate in the Chemistry Division, U.S. Naval Research Laboratory, Washington, DC 20375, USA

^b Chemistry Division, U.S. Naval Research Laboratory, Washington, DC 20375, USA. E-mail: debra.r.rolison.civ@us.navy.mil, megan.sassin@nrl.navy.mil

^c Materials Science & Technology Division, U.S. Naval Research Laboratory, Washington, DC 20375, USA

† Electronic supplementary information (ESI) available: Data from contact-angle measurements, impedance fits, and hydration numbers. See DOI: <https://doi.org/10.1039/d3lf00257h>



In an accompanying report, we demonstrate an iCVD-based route to a conformal ionic polymer coating on 2D and 1 mm thick 3D substrates, once poly(4-dimethylaminomethylstyrene), pDMAMS, is reacted with a di-halogen alkylating reagent to yield quaternary ammonium-containing pDMAMS⁺.²¹ We now evaluate the electrochemical properties of pDMAMS⁺ in various counterion forms for its use as an anion-conducting SSE. We find the films have potential charge-selective ion-regulation behavior, are electronically insulating, and display a range of anion conductivity based on anion identity and film hydration level. This combination of favorable properties renders the material a promising SSE for alkaline batteries such as AgO–Zn, NiOOH–Zn, and halide batteries such as AgCl–Zn, while the compatibility with non-line-of-sight deposition by iCVD opens the door to energy-dense 3D cells.

Results and discussion

Detailed synthesis and characterization of poly(4-dimethylaminomethylstyrene)-based films are described in our prior work,²¹ but are briefly summarized here. We use iCVD with an isomerically pure precursor, 4-dimethylaminomethylstyrene (4-DMAMS), to deposit films of pDMAMS on various planar or 3D substrates. The deposited films are annealed under vacuum at elevated temperature, which densifies the film and introduces a small amount of chemical cross-linking. We then convert 65% of the tertiary amines in the polymer to quaternary ammoniums through vapor-phase alkylation with 1-bromo-3-chloropropane to yield pDMAMS⁺ (Fig. 1). Prior characterization using nuclear magnetic resonance spectroscopy, attenuated total reflectance-Fourier transform infrared spectroscopy, and X-ray photoelectron spectroscopy confirm successful generation of quaternary ammonium groups and exchange of the Cl[−]/Br[−] counterion to anions of interest (Br[−], OH[−], or HCO₃[−]).²¹

The iCVD-deposited pDMAMS coatings are conformal on 2D and 3D substrates, nanoscopically smooth (<1 nm root mean square roughness), and have easily tuned thickness (30–1000+ nm). Mechanical measurements reveal that cross-linking increases the film's modulus. Grazing-incidence small and wide-angle X-ray scattering analyses of the various

film morphologies indicate the pDMAMS-based polymers are noncrystalline and that the charged forms pDMAMS⁺ and pDMAMS⁺(HCO₃[−]) contain ion-rich domains of distinct geometry.²¹ In light of these promising results, we turn to evaluating the electrochemical and electrical properties of the family of pDMAMS films on planar substrates.

Redox-probe assessment of pDMAMS and pDMAMS⁺ films

We use redox-probe voltammetry to assess molecular permeability of the conformal iCVD-derived, ~350 nm thick pDMAMS films. The voltammetric response of a pDMAMS-coated Au electrode in an aqueous potassium ferricyanide solution shows Fe²⁺/Fe³⁺ redox is present, but at lower current density compared to bare Au, revealing that as-deposited, uncharged pDMAMS is not entirely blocking (Fig. 2A). After annealing, however, the densified and lightly cross-linked pDMAMS completely blocks access of the anionic redox probe to the underlying Au electrode, confirming that the polymer coating is impermeable and pinhole free on a molecular level.

After conversion to pDMAMS⁺, the films remain pinhole free according to atomic force microscopy (AFM) measurements,²¹ but redox-probe assessment becomes more nuanced due to the hydrophilic nature of pDMAMS⁺. The dual-terminus alkylation reagent cross-links the pDMAMS film, ensuring that the polymer does not dissolve in water, but the film does take up water without delamination as evidenced by swelling and differences in water contact angle (Fig. S1 and S2[†]). As expected, pDMAMS⁺ allows a negatively charged redox probe to reach the electrode surface (Fig. 2B) while essentially no redox activity is recorded for a positively charged redox probe (hexaammineruthenium(III) chloride) compared to the bare Au electrode (Fig. 2C). Similar behavior is reported for films of the commercially available, styrenic anion-exchange membrane, Fumion®, which selectively reject a positively charged redox probe, but permit transport of a negatively charged redox probe to an underlying electrode surface for electroreduction.²² Our redox-probe results confirm that native, uncharged pDMAMS remains conformal after alkylation and that pDMAMS⁺ films confer charge-selective ion-transport behavior, an attractive property under further investigation.

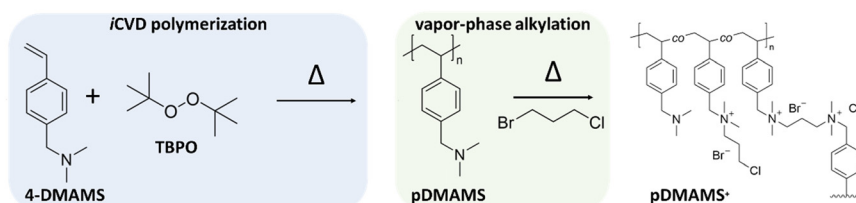


Fig. 1 Synthetic pathway for generating SSEs: iCVD is used to produce a thin coating of pDMAMS, which is then reacted with alkylating agent 1-bromo-3-chloropropane to yield pDMAMS⁺. The charge-balancing halide anions in pDMAMS⁺ are easily exchanged to other anions of interest using solution-based methods.



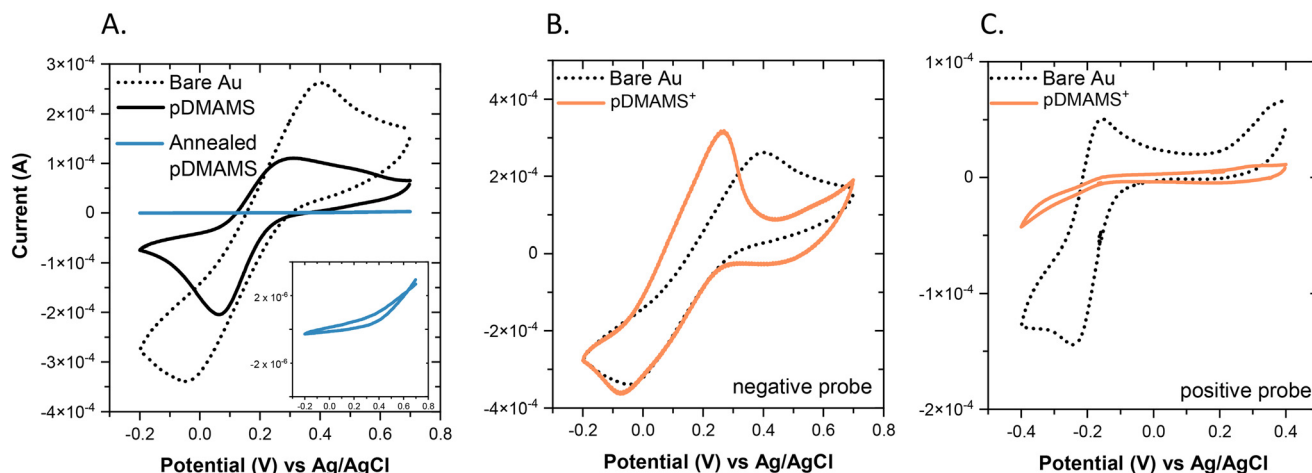


Fig. 2 Cyclic voltammograms (CVs) of bare Au and pDMAMS (or pDMAMS⁺)-coated Au electrodes (0.785 cm²) in aqueous KCl electrolyte: (A) 2 mM K₃[Fe(CN)₆]/0.1 M KCl; inset: expanded y-axis of annealed pDMAMS CV. (B) pDMAMS⁺ in 2 mM K₃[Fe(CN)₆]/0.1 M KCl. (C) pDMAMS⁺ in 1.0 mM hexaammineruthenium(III) chloride/1 M KCl. All CVs are taken at 50 mV s⁻¹.

Solid- and quasi-solid-state electrochemical properties of pDMAMS⁺ films

We next assess the electronic/ionic conductivity and voltage-stability windows of pDMAMS⁺(Br⁻), pDMAMS⁺(HCO₃⁻), and pDMAMS⁺(OH⁻) as a function of water content, either equilibrated in a nitrogen drybox (8% relative humidity (RH) designated “dry”) or after immersing in liquid water for 24 h. The two-terminal cell is fabricated by pressing an unmodified

stainless-steel spacer into a pDMAMS-coated stainless-steel spacer with sufficient pressure to ensure contact without shorting the cell. As shown by solid-state *i*-*V* sweeps from -100 mV to +100 mV, all three dry pDMAMS⁺ films demonstrate a MΩ linear response (Fig. 3A).²⁰ The calculated total electrical resistance of pDMAMS⁺(Br⁻), pDMAMS⁺(HCO₃⁻), and pDMAMS⁺(OH⁻) films is 20, 2, and 5 MΩ, respectively. While this method evaluates the total electrical resistance (ionic + electronic), the ionic contribution is small considering the nanoscale thickness of the film and the use of blocking electrodes. Further evaluation reveals $\sigma_{\text{electronic}} = 1.4 \times 10^{-11} \text{ S cm}^{-1}$ for pDMAMS⁺(Br⁻) (Fig. S3†). With these results, all anion-conducting forms of pDMAMS⁺ are sufficiently insulating to serve as the separator component in a 3D SSB.

All pDMAMS⁺(anion⁻) films are reductively stable to at least -1 V, with film failure indicated by a rise in current at ~-1.2 V (Fig. 3B). Scanning in the positive direction, the current begins to rise at +1.6–1.8 V, with film failure occurring at ~+2.2 V for the pDMAMS⁺(Br⁻) and pDMAMS⁺(HCO₃⁻) films. The pDMAMS⁺(OH⁻) film is stable up to ~+3 V with total failure occurring around +3.3 V. The varied voltage-stability values may relate to differences in the networks induced by ion-exchange procedures and/or electrode/anion corrosion potential. The solid-state electrochemical window displayed by each pDMAMS⁺(anion⁻) form is sufficiently wide, however, to withstand voltage windows characteristic of such anion-mediated energy-storage chemistries as Ag–Zn (1.9 V), Ni–Zn (1.7 V) and Zn–Br (1.9 V),²³ and those of alkaline fuel cells.

With the electronic conductivity suitably low and the electrochemical stability window sufficiently wide, we extract the average ionic conductivity of pDMAMS⁺(anion⁻) films as a function of hydration *via* electrochemical impedance spectroscopy (EIS) modeled using equivalent circuits. The model for the dry films is a QR circuit (Fig. 4A), where the *Q* element represents the nonideal capacitive nature of the film

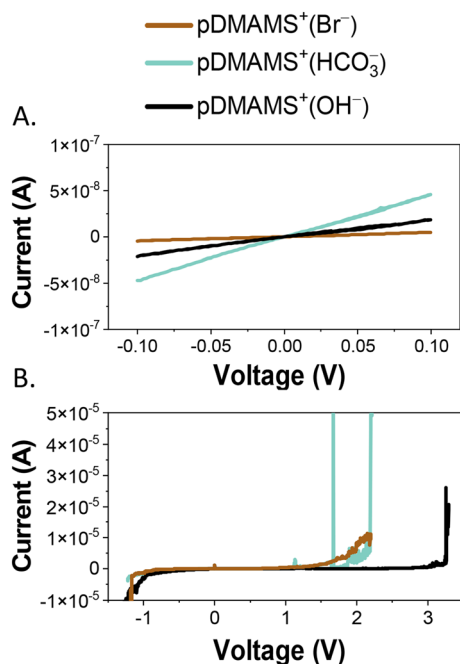


Fig. 3 (A) Electrical conductivity assessment of pDMAMS⁺ films using linear-sweep voltammetry. (B) Voltage window for the pDMAMS⁺ films measured from 0 V using positive and negative linear sweeps to the onset of breakdown current. A fresh cell is used for each sweep direction and the positive and negative branches are then combined to assess electrochemical stability.



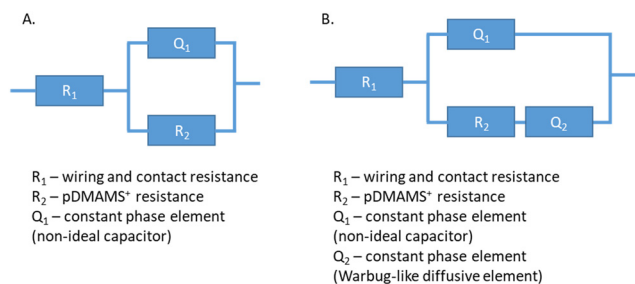


Fig. 4 Equivalent-circuit models for EIS data: (A) 8% RH pDMAMS⁺(anion[−]) films; and (B) water-swelled pDMAMS⁺(anion[−]) films.

and R_2 the ionic resistance of the film from which conductivity is calculated according to the following:

$$\sigma = \frac{1}{R_2} \times \frac{t}{A}, \quad (1)$$

where t is the film thickness and A is the geometric area of the iCVD-coated stainless-steel spacer. Such a circuit is appropriate to model ion conduction in solid-state electrolytes, which can lack the Warburg-like diffusive element seen in traditional liquid electrolytes.^{15,24} The model for the swelled, water-wet films (quasi-solid-state) adds another Q element (Q_2) that accounts for non-ideal Warburg-like diffusive behavior seen in the low-frequency regime (Fig. 4B).

The model-fit results for each element are shown in Fig. 5A and B with the average values compiled in Table 1 (the fits for individual measurements are found in Tables S1 and S2†). In general, the Q_1 capacitance of the OH[−]-compensated polymer is slightly higher than that for the Br[−] and HCO₃[−]-compensated polymers, with all forms (wet and dry) close to ideal capacitance (>0.85, with 1.0 being ideal). Deviation from ideal Warburg behavior is seen for all water-swelled films, which may stem from a breakdown in the semi-infinite diffusion assumption, *i.e.*, tortuosity and/or narrowing/broadening of the ion-transport pathway.^{25–27}

As these films contain tethered positive charges and no free salt, the ionic conductivity values shown in Fig. 5C and Table 1 are entirely derived from single-ion transport, in this case single anion. In all cases, the water-swelled conductivity exceeds that of the 8% RH condition by two orders of magnitude, with the relative increase in conductivity greatest for the Br[−] form and lowest for the OH[−] form.

Ion-pair dissociation in pDMAMS⁺ films and the related difference in water uptake depend on the incorporated anion, which can explain the differences in ionic conductivity. The uptake of water by pDMAMS⁺(anion[−]) increases the number of dissociated charge carriers and increases their mobility through vehicular ion transport and enlarging the cross section of the ion-transport channel.²⁸ We turn to molecular dynamic (MD) simulations to probe the diffusion of OH[−] in pDMAMS⁺ as a function of water content, where the number of water molecules per charge carrier, λ is defined as the number of water molecules per ammonium ions [$n(\text{H}_2\text{O})/(\text{N}^+)$]. We first consider the distribution of OH[−] mean square displacement (MSD) in a simulated dry film where $\lambda = 0$ (Fig. 6A).

The computational MSD is best fit using two diffusion constants, a result that holds for each λ studied. Two major populations of OH[−] thus exist: one where slower moving OH[−] strongly interacts with the tethered N⁺ (characterized by diffusion constant D_1) and a second where faster moving OH[−] does not interact with N⁺ (characterized by diffusion constant D_2). For all λ , $D_2 > D_1$, but both are relatively invariant for $\lambda = 0$ –3 and increase markedly at $\lambda > 3$ (Fig. 6B), a result consistent with the improved conductivity measured for the water-swelled films (Fig. 5C). While perhaps not directly comparable to the thin-film format, we experimentally find $\lambda \approx 0.5$ –3 when vapor-phase equilibrating bulk-synthesized pDMAMS⁺(Br[−]) under RH conditions set by saturated salt solutions (from 11% (LiCl_(aq)) to 97% (K₂SO_{4(aq)}); $\lambda \approx 5$ for liquid water-wet films (Fig. S2†).

The thickness of water-wet pDMAMS⁺(HCO₃[−]) and pDMAMS⁺(OH[−]) films expands about four-fold compared to swelled pDMAMS⁺(Br[−]) films, where the latter is visibly more

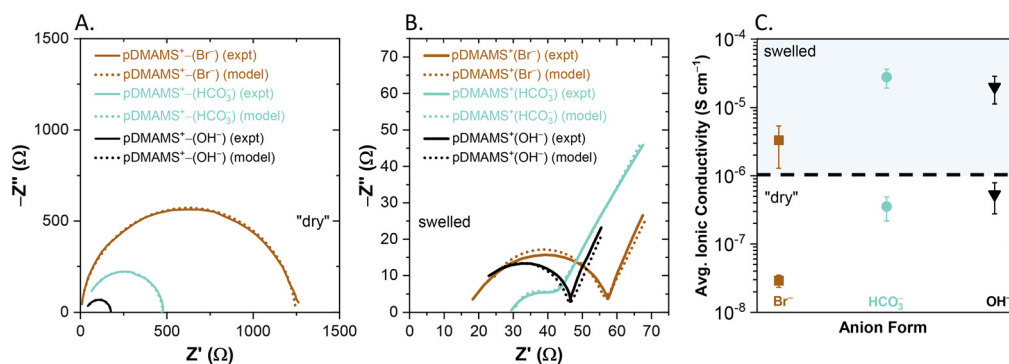


Fig. 5 (A) Representative EIS spectra for dry (8% RH equilibrated) pDMAMS⁺(anion[−]) films. (B) Representative EIS spectra for water-swelled pDMAMS⁺(anion[−]) films. (C) Ionic conductivity of pDMAMS⁺(anion[−]) films, either swelled directly with water or equilibrated at 8% RH. Error bars are standard deviation of EIS-calculated ionic conductivity for three or more different samples propagated with error associated with measuring film thickness.



Table 1 Listed electrical values and thickness used to calculate ionic conductivity for iCVD-derived pDMAMS⁺-based electrolytes

Composition	Electronic resistance at 8% RH (MΩ)	Voltage stability window at 8% RH (V)	σ at 8% RH (S cm ⁻¹)	Thickness (<i>t</i>) at 8% RH (nm)	σ water-swelled (S cm ⁻¹)	Thickness (<i>t</i>) water-swelled (nm)
pDMAMS ⁺ (Br ⁻)	20	~1 to 1.6	$2.5 \times 10^{-8} \pm 6.0 \times 10^{-9}$	580 ± 59	$3.3 \times 10^{-6} \pm 2.0 \times 10^{-6}$	1000 ± 500
pDMAMS ⁺ (HCO ₃ ⁻)	2	~1 to 1.8	$3.5 \times 10^{-7} \pm 1.3 \times 10^{-7}$	502 ± 83	$2.8 \times 10^{-5} \pm 8.4 \times 10^{-6}$	2500 ± 500
pDMAMS ⁺ (OH ⁻)	5	~1 to 3	$5.3 \times 10^{-7} \pm 1.7 \times 10^{-7}$	502 ± 83	$2.0 \times 10^{-5} \pm 8.6 \times 10^{-6}$	2500 ± 500

hydrophobic in terms of de-wetting and water contact angle (Fig. S1†). Higher water content in the film also affects ion structural arrangement. As indicated by our grazing-incidence X-ray scattering analyses of pDMAMS and pDMAMS⁺,²¹ the looser packing of ions in pDMAMS⁺(HCO₃⁻) should facilitate ion dissociation, water uptake, and favorable transport domain formation. The swelled HCO₃⁻ form is consistently more ionically conductive than the OH⁻ form, a result predicted by recent MD simulations conducted by our group.²⁹ Although HCO₃⁻ is bulkier than OH⁻ (anion + first shell is 2.7 Å for OH⁻, 3.33 Å for Br⁻, and 3.5 Å for HCO₃⁻), the bicarbonate anion has a lower charge density due to resonance-stabilized charge delocalization.^{30–33} When sufficient film hydration and large enough ion-transport domains exist, the positive impact of lower anionic charge density may outweigh the negative impact of bulkiness on anion mobility. The multi-faceted impact of water content on SSE conductivity, in which it influences polymer morphology,

charge screening, ion dissociation, and ion transport mechanisms, make hydration an important design metric for future anionic SSEs.

The ionic conductivity of pDMAMS⁺(HCO₃⁻) and pDMAMS⁺(OH⁻) exceeds 10⁻⁵ S cm⁻¹ in the water-swelled state, which is one to three orders of magnitude lower than the conductivity reported for most alkaline-exchange membranes (AEMs) of similar ion-exchange capacity (IEC).³⁴ One explanation for this result is that while most AEMs are 10s to 100 s of microns thick or more, the nanoscale nature of the iCVD-generated pDMAMS⁺ films may impose confinement effects (such as altered chain rigidity and network morphology relative to bulk-synthesized polymer) that impact ion transport.^{35,36} In pDMAMS⁺, the tethered ammonium cations directly participate in cross-linking the polymer chains (Fig. 1), which will also lower the conductivity by reducing the degrees of freedom at the charged sites. Experiments on chemically similar SSEs where the ionic groups are not participating in cross-links are currently underway.

While the conductivity of these SSEs at 8% RH is low compared to the conventional minimum ionic conductivity required of bulk polymer electrolytes (10⁻⁴ S cm⁻¹), the total contribution to cell resistance from a submicron-thick electrolyte is less than traditional, microns-thick electrolytes. Another countervailing factor comes from the fact that the pDMAMS⁺ series display single (an)ion conduction. The low total resistance contribution and the single-ion conducting nature of the electrolytes counterbalance the low solid-state conductivity with respect to use in a practical cell. In conjunction with efforts to improve iCVD-generated SSE conductivity, these promising results demonstrate the first anion-conducting SSE generated *via* post-deposition modification of an iCVD-based polymer and lay the groundwork for 3D SSBs based on non-Li-ion chemistries.

Conclusions

A series of single anion-conducting polymer electrolytes based on quaternized pDMAMS are synthesized using iCVD, a non-line-of-sight technique. The various forms of the pDMAMS films are found to be pinhole free, thwart redox-probe permeation, and demonstrate charge-selective rejection. Electrochemical impedance spectroscopy and subsequent model fitting reveal that the single-ion conductivity of the pDMAMS SSEs, ranging from 10⁻⁸ to 10⁻⁵ S cm⁻¹, depends on hydration level and counter-anion

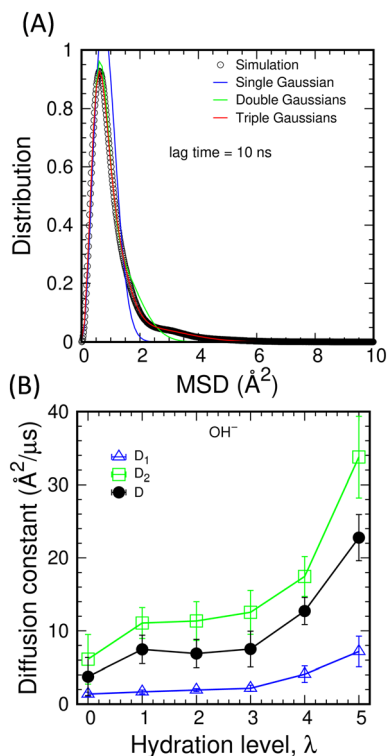


Fig. 6 (A) Distribution of OH⁻ mean square displacement in pDMAMS⁺(OH⁻) for $\lambda = 0$. (B) Diffusion constants for slower N⁺-bound OH⁻ (D_1), faster unbound OH⁻ (D_2), and average.



identity. The least conductive pDMAMS⁺(anion[−]) version is Br[−] compensated and dehydrated, while the most conductive version is HCO₃[−] compensated and water swelled. As the highest conductivity is obtained in the water-swelled quasi-solid-state form, future work will investigate the impact of hydration on device performance. The single-ion conductivity values, in conjunction with the submicron-scale thickness, electronically insulating nature, and wide solid-state voltage-stability window establish pDMAMS chemistry as suitable for use as a solid-state electrolyte for next-generation beyond-Li-ion alkaline batteries.

Experimental

Water used in all measurements and reactions was 18 MΩ-cm (Thermo Scientific Barnstead MicroPure).

Synthesis of 4-dimethylaminomethylstyrene monomer (4-DMAMS) and iCVD-generated films

Detailed synthesis of isomerically pure 4-DMAMS, generation of pDMAMS films *via* iCVD, and post-deposition modifications are detailed in our previous work.²¹ For redox-probe measurements, films are deposited on gold-coated glass slides (25 mm × 35 mm). For all other electrochemical measurements, films are deposited on stainless-steel spacers (MTI Corp.).

Film thickness/profilometry

All iCVD-generated pDMAMS films in this study are on the order of 350 nm thick. Dry-film thickness was measured as previously described using profilometry.²¹ The thickness of water-swelled films was measured as follows. The various pDMAMS⁺ films coated on stainless-steel spacers were swelled in water for 24 h. Another blank spacer was placed in direct contact with the pDMAMS⁺ film, and the total thickness was measured with a digital micrometer. The error was taken to be ±0.5 μm.

Contact-angle measurements

Contact-angle measurements were performed on various pDMAMS films coated on stainless-steel spacers using a Biolin Theta Flex. Dispensed water volume was 4 μL and measurements were taken at set time intervals, with each measurement taken at least in triplicate on a fresh section of sample.

Water-uptake (λ) measurements

A thin glass slide was cleaned, weighed, and coated with a thick layer of bulk-synthesized pDMAMS by drop casting from a 20 wt% solution in xylenes. After drying under vacuum at 100 °C, the pDMAMS films were quaternized with 1-bromo-3-chloropropane in the vapor phase as described previously.²¹ The dried pDMAMS⁺ films were subsequently equilibrated over P₂O₅ for 24 h in a sealed vessel to quantitatively dehydrate the sample. The dehydrated samples

were weighed and then equilibrated in the vapor of saturated aqueous salt solutions of successively higher relative humidity: LiCl (11.3% RH), MgCl₂ (33% RH), Mg(NO₃)₂ (53% RH), (NH₄)₂SO₄ (81% RH), and K₂SO₄ (97% RH). Samples were equilibrated over each solution for 24 h and quickly weighed after removing from the sealed container before transferring to a new container with a new solution. To finish the water-uptake series, samples were immersed in deionized water for 16 h, removed, patted dry, and quickly weighed. From the water uptake, the value of λ, for $\lambda = n(\text{H}_2\text{O})/(\text{N}^+)$, was calculated.

Electrochemical measurements

All electrochemical measurements were performed using a Gamry Instruments Reference 620 potentiostat.

The substrates used for all redox-probe measurements were Au-coated glass slides serving as the working electrode *versus* platinum wire counter and Ag/AgCl reference electrodes. The working electrode area was an o-ring-defined circle of 1 cm diameter (0.785 cm²). For a negatively charged redox probe, a freshly prepared aqueous solution of 0.1 M potassium chloride (KCl, Sigma, Reagent Plus) + 2 mM potassium ferricyanide (Sigma, ACS Reagent Grade) was used. The potential is swept between −0.2 V to 0.7 V *vs.* Ag/AgCl at a scan rate of 50 mV s^{−1}. For a positively charged redox probe, a freshly prepared aqueous solution of 1.0 M KCl + 1.0 mM hexaammineruthenium(III) chloride (Aldrich, 98%) was used.²¹ The potential was swept between −0.4 V and 0.4 V *vs.* Ag/AgCl at a scan rate of 50 mV s^{−1}.

The ionic conductivity of pDMAMS films was obtained from fitting electrochemical impedance spectroscopy data using appropriate equivalent-circuit models. The frequency range of analysis was generally 4 MHz to 0.1 Hz but the data were truncated for model fitting. All films used for ionic conductivity measurement were deposited onto stainless-steel spacers (15 mm diameter, MTI Corp.). Films designated “dry” were measured within a nitrogen box under a controlled relative humidity of 8%. The measurement was taken by placing an unmodified stainless-steel spacer electrode in direct contact with the pDMAMS⁺-coated electrode. Using a C-clamp, the electrodes were pressed together as much as possible without short circuiting to ensure good interfacial contact. For water-swelled ionic conductivity, the various films were soaked in 18 MΩ cm water (O₂ and CO₂ pre-removed *via* N₂ purge) for 24 h prior to analysis. Swelled films were measured in the same method as above, but with the addition of a polyethylene donut separator (15 μm thick, 7/16 in diameter hole) that prevents direct contact between the pDMAMS⁺-coated electrode and the counter electrode. Additional water was added to the center of the donut separator prior to cell assembly to ensure good interfacial contact and prevent film dewetting. Nyquist plots were fit with equivalent-circuit models using the Gamry Echem Analyst software package.



The voltage stability window was determined by employing linear-scan voltammetry in either the negative or positive direction at a rate of 10 mV s^{-1} , with a new sample used for each scan direction. Total electrical conductivity was similarly assessed, but by sweeping the voltage at 5 mV s^{-1} . The electrical resistance was calculated by taking the inverse of the slope of the ohmic response obtained by cyclic voltammetry.

Molecular dynamics simulations

Initial structures of 24 pDMAMS⁺ chains of 20 repeat units are constructed in an $8 \times 8 \times 8 \text{ nm}$ cubic box using Moltemplate.³⁷ Hydroxide ions are added as counterions to neutralize the system. For simulations at different hydration levels, water molecules are added to the box after equilibration at 300 K. The number of water molecules in the system is established by the hydration number as the ratio of water molecules to OH[−]. All atom force-field parameters for pDMAMS⁺, OH[−], and water molecules are described in our previous work.²⁹

All MD simulations are performed using Gromacs 5.1.5 package³⁸ with periodic boundary conditions in three dimensions. Initial structures are energy-minimized to remove any steric clash between atoms by the steepest descent algorithm. To ensure random starting configurations with well-mixed polymer chains, the systems are simulated for 10 ns in the NVT (constant volume and temperature) ensemble at an elevated temperature of 800 K. Langevin dynamics with a coupling time constant of 2 ps is used to control the temperature. After another 10 ns NPT (constant pressure and temperature) run to achieve the desired volume at 1 atm, a simulated annealing procedure is applied to the systems to lower the temperature down to 300 K using the Berendsen barostat³⁹ to control the pressure with the coupling time constant of 2 ps. Finally, the systems are simulated for 1 μs in the NPT ensemble with the Parrinello–Rahman barostat⁴⁰ with a time constant of 2 ps and saving the trajectories every 100 ps for further analysis. Details of the simulation protocol can be found in ref. 28.

Author contributions

Hunter O. Ford: conceptualization, data curation, formal analysis, investigation, methodology, validation, visualization, writing – original draft, writing – review and editing. Brian L. Chaloux: conceptualization, data curation, formal analysis, investigation, methodology, validation, writing – review and editing. Youngchan Kim: data curation, formal analysis, investigation, writing – review and editing. Jeffrey W. Long: conceptualization, resources, validation, writing – review and editing. Debra R. Rolison: conceptualization, validation, formal analysis, funding acquisition, writing – review and editing. Megan B. Sassin: conceptualization, validation, formal analysis, funding acquisition, writing – review and editing.

Conflicts of interest

The authors have no conflicts to declare.

Acknowledgements

This research was supported by the U.S. Office of Naval Research. H. O. F. is an NRL–National Research Council postdoctoral associate (2022–2024).

References

- 1 J. W. Long, B. Dunn, D. R. Rolison and H. S. White, Three-Dimensional Battery Architectures, *Chem. Rev.*, 2004, **104**, 4463–4492.
- 2 J. W. Long, C. P. Rhodes, A. L. Young and D. R. Rolison, Ultrathin, Protective Coatings of Poly(o-Phenylenediamine) as Electrochemical Proton Gates: Making Mesoporous MnO₂ Nanoarchitectures Stable in Acid Electrolytes, *Nano Lett.*, 2003, **3**, 1155–1161.
- 3 A. Pearce, T. Schmitt, E. Sahadeo, D. M. Stewart, A. Kozen, K. Gerasopoulos, A. A. Talin, S. B. Lee, G. W. Rubloff and K. E. Gregorczyk, Three-Dimensional Solid-State Lithium-Ion Batteries Fabricated by Conformal Vapor-Phase Chemistry, *ACS Nano*, 2018, **12**, 4286–4294.
- 4 T. S. Arthur, D. J. Bates, N. Cirigliano, D. C. Johnson, P. Malati, J. M. Mosby, E. Perre, M. T. Rawls, A. L. Prieto and B. Dunn, Three-Dimensional Electrodes and Battery Architectures, *MRS Bull.*, 2011, **36**, 523–531.
- 5 M. Roberts, P. Johns, J. Owen, D. Brandell, K. Edstrom, G. El Enany, C. Guery, D. Golodnitsky, M. Lacey, C. Lecoeur, H. Mazor, E. Peled, E. Perre, M. M. Shaijumon, P. Simon and P.-L. Taberna, 3D Lithium Ion Batteries—From Fundamentals to Fabrication, *J. Mater. Chem.*, 2011, **21**, 9876–9890.
- 6 J. Cho, M. D. Losego, H. G. Zhang, H. Kim, J. M. Zuo, I. Petrov, D. G. Cahill and P. V. Braun, Electrochemically Tunable Thermal Conductivity of Lithium Cobalt Oxide, *Nat. Commun.*, 2014, **5**, 4035.
- 7 X. F. Wu, J. Lee, V. Varshney, J. L. Wohlwend, A. K. Roy and T. F. Luo, Thermal Conductivity of Wurtzite Zinc-Oxide from First-Principles Lattice Dynamics – A Comparative Study with Gallium Nitride, *Sci. Rep.*, 2016, **6**, 22504.
- 8 D. R. Lide, *CRC Handbook of Chemistry and Physics*, CRC Press, Boca Raton, FL, 85th edn, 2004, Section 12, p. 218.
- 9 J. F. Parker, C. N. Chervin, E. S. Nelson, D. R. Rolison and J. W. Long, Wiring Zinc in Three Dimensions Re-writes Battery Performance—Dendrite-free Cycling, *Energy Environ. Sci.*, 2014, **7**, 1117–1124.
- 10 J. F. Parker, E. S. Nelson, M. D. Wattendorf, C. N. Chervin, J. W. Long and D. R. Rolison, Retaining the 3D Framework of Zinc Sponge Anodes upon Deep Discharge in Zn–Air Cells, *ACS Appl. Mater. Interfaces*, 2014, **6**, 19471–19476.
- 11 J. F. Parker, C. N. Chervin, I. R. Pala, M. Machler, M. F. Burz, J. W. Long and D. R. Rolison, Rechargeable Nickel-3D Zinc Batteries: An Energy-Dense, Safer Alternative to Lithium-Ion, *Science*, 2017, **356**, 414–417.



- 12 B. J. Hopkins, M. B. Sassin, C. N. Chervin, P. A. DeSario, J. F. Parker, J. W. Long and D. R. Rolison, Fabricating Architected Zinc Electrodes with Unprecedented Volumetric Capacity in Rechargeable Alkaline Cells, *Energy Storage Mater.*, 2020, **27**, 370–376.
- 13 P. Moni, A. Al-Obeidi and K. K. Gleason, Vapor Deposition Routes to Conformal Polymer Thin Films, *Beilstein J. Nanotechnol.*, 2017, **8**, 723–735.
- 14 S. H. Baxamusa, S. G. Im and K. K. Gleason, Initiated and Oxidative Chemical Vapor Deposition: A Scalable Method for Conformal and Functional Polymer Films on Real Substrates, *Phys. Chem. Chem. Phys.*, 2009, **11**, 5227–5240.
- 15 N. Chen, B. Reeja-Jayan, J. Lau, P. Moni, A. D. Liu, B. Dunn and K. K. Gleason, Nanoscale, Conformal Polysiloxane Thin Film Electrolytes for Three-Dimensional Battery Architectures, *Mater. Horiz.*, 2015, **2**, 309–314.
- 16 A. M. Coclite, P. Lund, R. Di Mundo and F. Palumbo, Novel Hybrid Fluoro-Carboxylated Copolymers Deposited by Initiated Chemical Vapor Deposition as Protonic Membranes, *Polymer*, 2013, **54**, 24–30.
- 17 C. Ranacher, R. Resel, P. Moni, B. Cermenek, V. Hacker and A. M. Coclite, Layered Nanostructures in Proton Conductive Polymers Obtained by Initiated Chemical Vapor Deposition, *Macromolecules*, 2015, **48**, 6177–6185.
- 18 M. H. Wang, X. X. Wang, P. Moni, A. D. Liu, D. H. Kim, W. J. Jo, H. Sojoudi and K. K. Gleason, CVD Polymers for Devices and Device Fabrication, *Adv. Mater.*, 2017, **29**, 1604606.
- 19 Y. Yoo, B. G. Kim, K. Pak, S. J. Han, H. S. Song, J. W. Choi and S. G. Im, Initiated Chemical Vapor Deposition (iCVD) of Highly Cross-Linked Polymer Films for Advanced Lithium-Ion Battery Separators, *ACS Appl. Mater. Interfaces*, 2015, **7**, 18849–18855.
- 20 M. B. Sassin, J. W. Long, J. M. Wallace and D. R. Rolison, Routes to 3D Conformal Solid-State Dielectric Polymers: Electrodeposition Versus Initiated Chemical Vapor Deposition, *Mater. Horiz.*, 2015, **2**, 502–508.
- 21 H. O. Ford, B. L. Chaloux, M. W. Swift, C. A. Klug, J. B. Miller, B. Jugdersuren, X. Zuo, J. W. Long, X. Liu, M. D. Johannes, D. R. Rolison and M. B. Sassin, Non-Line-of-Sight Synthesis and Characterization of a Conformal Submicron-Thick Cationic Polymer Deposited on 2D and 3D Substrates, *RSC Appl. Interfaces*, 2024, **1**, DOI: [10.1039/d3lf00256j](https://doi.org/10.1039/d3lf00256j).
- 22 J. H. Xu, J. Leddy and C. Korzeniewski, Cyclic Voltammetry as a Probe of Selective Ion Transport within Layered, Electrode-Supported Ion-Exchange Membrane Materials, *J. Electrochem. Soc.*, 2022, **169**, 026520.
- 23 D. Linden, K. W. Beard and T. B. Reddy, *Linden's Handbook of Batteries*, McGraw-Hill, 2019.
- 24 P. Vadhva, J. Hu, M. J. Johnson, R. Stocker, M. Braglia, D. J. L. Brett and A. J. E. Rettie, Electrochemical Impedance Spectroscopy for All-Solid-State Batteries: Theory, Methods and Future Outlook, *ChemElectroChem*, 2021, **8**, 1930–1947.
- 25 S. J. Cooper, A. Bertei, D. P. Finegan and N. P. Brandon, Simulated Impedance of Diffusion In Porous Media, *Electrochim. Acta*, 2017, **251**, 681–689.
- 26 T. Y. Soboleva, Z. Xie, Z. Q. Shi, E. Tsang, T. C. Navessin and S. Holdcroft, Investigation of the Through-Plane Impedance Technique for Evaluation of Anisotropy of Proton Conducting Polymer Membranes, *J. Electroanal. Chem.*, 2008, **622**, 145–152.
- 27 F. Pouraghajan, H. Knight, M. Wray, B. Mazzeo, R. Subbaraman, J. Christensen and D. Wheeler, Quantifying Tortuosity of Porous Li-Ion Battery Electrodes: Comparing Polarization-Interrupt and Blocking-Electrolyte Methods, *J. Electrochem. Soc.*, 2018, **165**, A2644–A2653.
- 28 H. O. Ford, B. Park, J. Z. Jiang, M. E. Seidler and J. L. Schaefer, Enhanced Li⁺ Conduction within Single-Ion Conducting Polymer Gel Electrolytes via Reduced Cation-Polymer Interaction, *ACS Mater. Lett.*, 2020, **2**, 272–279.
- 29 Y. C. Kim, B. L. Chaloux, D. R. Rolison, M. D. Johannes and M. B. Sassin, Molecular Dynamics Study of Hydroxide Ion Diffusion in Polymer Electrolytes, *Electrochem. Commun.*, 2022, **140**, 107334.
- 30 P. D'Angelo, V. Migliorati and L. Guidoni, Hydration Properties of the Bromide Aqua Ion: the Interplay of First Principle and Classical Molecular Dynamics, and X-Ray Absorption Spectroscopy, *Inorg. Chem.*, 2010, **49**, 4224–4231.
- 31 M. Smiechowski and J. Stangret, Hydroxide Ion Hydration in Aqueous Solutions, *J. Phys. Chem. A*, 2007, **111**, 2889–2897.
- 32 P. P. Kumar, A. G. Kalinichev and R. J. Kirkpatrick, Hydrogen-Bonding Structure and Dynamics of Aqueous Carbonate Species from Car-Parrinello Molecular Dynamics Simulations, *J. Phys. Chem. B*, 2009, **113**, 794–802.
- 33 S. Chowdhuri and A. Chandra, Dynamics of Halide Ion-Water Hydrogen Bonds in Aqueous Solutions: Dependence on Ion Size and Temperature, *J. Phys. Chem. B*, 2006, **110**, 9674–9680.
- 34 S. Maurya, S. H. Shin, Y. Kim and S. H. Moon, A Review on Recent Developments of Anion Exchange Membranes for Fuel Cells and Redox Flow Batteries, *RSC Adv.*, 2015, **5**, 37206–37230.
- 35 S. A. Eastman, S. Kim, K. A. Page, B. W. Rowe, S. H. Kang, S. C. DeCaluwe, J. A. Dura, C. L. Soles and K. G. Yager, Effect of Confinement on Structure, Water Solubility, and Water Transport in Nafion Thin Films, *Macromolecules*, 2012, **45**, 7920–7930.
- 36 Q. J. Zhao, P. Bennington, P. F. Nealey, S. N. Patel and C. M. Evans, Ion Specific, Thin Film Confinement Effects on Conductivity in Polymerized Ionic Liquids, *Macromolecules*, 2021, **54**, 10520–10528.
- 37 A. I. Jewett, D. Stelter, J. Lambert, S. M. Saladi, O. M. Roscioni, M. Ricci, L. Autin, M. Maritan, S. M. Bashusqeh, T. Keyes, R. T. Dame, J. Shea, G. J. Jensen and D. S. Goodsell, Moltemplate: A Tool for Coarse-Grained Modeling of Complex Biological Matter and Soft Condensed Matter Physics, *Mol. Biol.*, 2021, **433**, 166841.
- 38 D. Van der Spoel, E. Lindahl, B. Hess, G. Groenhof, A. E. Mark and H. J. C. Berendsen, GROMACS: Fast, Flexible, and Free, *J. Comput. Chem.*, 2005, **26**, 1701–1718.



- 39 H. J. C. Berendsen, J. P. M. Postma, W. F. Vangunsteren, A. Dinola and J. R. Haak, Molecular-Dynamics with Coupling to an External Bath, *J. Chem. Phys.*, 1984, **81**, 3684–3690.
- 40 M. Parrinello and A. Rahman, Polymorphic Transitions in Single-Crystals – A New Molecular-Dynamics Method, *J. Appl. Phys.*, 1981, **52**, 7182–7190.

